Advances in Water Resources 203 (2025) 105022

Contents lists available at ScienceDirect

Advances in Water Resources

journal homepage: www.elsevier.com/locate/advwatres

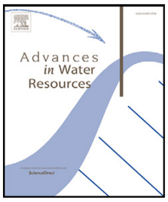

Homogenization-informed convolutional neural network to predict permeability and dispersion in porous media

Ross M. Weber, Ilenia Battiato *

Department of Energy Science and Engineering, Stanford University, Stanford, CA 94305, USA

ARTICLE INFO

Keywords:
Permeability
Dispersion
Closure problem
Convolutional neural networks

ABSTRACT

Understanding the transport properties of fluids through porous media is crucial in a wide range of scientific and engineering applications. Accurately predicting key parameters, such as permeability and effective dispersion, is essential for optimizing these processes. These parameters depend not only on the pore-scale geometry but also on flow conditions, and are traditionally expensive to compute since they are generally determined by solving direct numerical simulations on macroscopic pore-scale domains. Such computational costs limit the effectiveness of data-driven approaches in terms both of predictive accuracy and/or types of geometries that can be accurately handled. This is because the computational cost for training over a broad set of topologies and dynamic conditions is prohibitive. In this work, we propose an approach that combines deep learning with multiscale modeling techniques, and exploits the computational efficiency of homogenization theory for periodic domains to support a data-driven technique. By using only a unit cell for training purposes, we are able to generate a large dataset of porous media images and corresponding permeability and dispersion tensors at a significantly reduced computational cost, while spanning an unprecedented range of the geometric and dynamic parameter space. The dataset is composed of 10,000 images, is designed to include a wide variety of morphological properties and serves as the training set for a Convolutional Neural Network (CNN) that estimates permeability and dispersion tensors from both microstructural images and input flow conditions described by the Péclet number. The CNN can quickly and accurately characterize effective properties (permeability and dispersion tensors) spanning more than three orders of magnitude for a wide range of pore-scale topologies and flow regimes. These results highlight the potential to enhance porous media characterization and prediction in various fields.

1. Introduction

The study of fluid transport properties in porous media plays a vital role in various scientific and engineering domains, encompassing carbon sequestration (Honari et al., 2016; Hidalgo and Carera, 2009), pollutant transport (Meigel et al., 2022; Ling et al., 2016), enhanced oil recovery (Wang et al., 2021b; Carbonell and Whitaker, 1983), and ecohydrology applications (Rubol et al., 2016; Ling et al., 2021). Two key parameters of interest for these systems are the permeability and effective dispersion tensors. When inertial effects at the pore-scale are negligible, permeability depends solely on the geometry of the porous medium whereas dispersion additionally depends on flow conditions, described by the Péclet number, which relates advective and diffusive time scales (Nguyen and Papavassiliou, 2020). In presence of non-negligible inertia, such relationships become more complex with permeability exhibiting nonlinear dependency on Reynolds number, and the dispersion tensor being proportional to both Reynolds and Péclet numbers (Wood, 2007). Beside characterization experiments, traditional "synthetic" approaches for calculating these parameters often entail numerical simulations of flow and transport through large and complex microstructures, which is computationally expensive because it requires resolving the intricate details of the pore-scale geometry over a domain of macroscopic size with hundreds or thousands of pores (Icardi et al., 2014; Gouze et al., 2021; Yang et al., 2016). Alternatively, researchers have commonly resorted to analytical and empirical relationships to approximate these properties. These include the Kozeny–Carman equation for permeability estimation (Carman, 1997) and similar relationships that predict dispersion as a function of Péclet number (e.g., van Milligen and Bons, 2012). However, relying solely on such relationships can lead to inaccuracies, as the complex interplay of various physical phenomena governing fluid flow and solute transport through porous structures may not always be adequately captured by these simplified relationships, particularly when

---

* Corresponding author.
E-mail address: ibattiat@stanford.edu (I. Battiato).

https://doi.org/10.1016/j.advwatres.2025.105022
Received 26 July 2024; Received in revised form 9 May 2025; Accepted 30 May 2025

dealing with complex morphologies. As a result, there is a pressing need for more advanced and accurate approaches that overcome the limitations of traditional analytical and empirical models but maintain computational efficiency.

In recent years, machine learning methods generally (Taghizadeh et al., 2022), and Convolutional Neural Networks (CNNs) specifically have emerged as a promising tool of achieving this task of efficient characterization of both 2D and 3D porous media (Rao and Liu, 2020; Yang et al., 2018; Lu et al., 2019). Despite the computational cost of training, the main advantage of using CNN to predict effective properties is that CNN's predictions (in 2D or 3D) have proved to be more accurate for realistically complex structures, when appropriately trained, compared to classical analytical/empirical correlations. A computational alternative to CNNs would be direct numerical simulations (DNS) of flow and transport in each and every structure for which effective parameters need to be evaluated: when very many evaluations need to be performed, the computational cost will increase, and pre-trained CNNs provide a better alternative to either approach (empirical models or DNS simulations) both in terms of computational cost and predictive accuracy. These deep learning models leverage the power of convolutional layers to effectively extract spatial features from porous media images and learn complex relationships between microstructure and properties. Several studies have successfully employed CNNs for predicting porous media parameters such as tortuosity, permeability, conductivity, etc. (e.g., Wu et al., 2019; Wang et al., 2020; Graczyk and Matyka, 2020; Kamrava et al., 2020; Wang et al., 2021a; Marcato et al., 2021, 2022; Weber et al., 2022; Marcato et al., 2023; Špetlík et al., 2024; Tang et al., 2022). For instance, Marcato et al. (2021, 2022) developed a CNN-based approach to estimate permeability and filtration rate from generated spherical particle packings, achieving high prediction accuracy. Hanna et al. (2024) similarly developed a CNN model for permeability prediction using macroscale fibrous porous media images and injection experiments as the training data. Additionally, Kamrava et al. (2021) utilized a CNN architecture to predict longitudinal dispersion of porous media structures. These works demonstrate the potential of CNNs to capture the intricate relationships between morphology and transport properties.

However, because of the computational cost associated with direct numerical simulations of flow and transport in pore-scale domains of macroscopic size, restrictive constraints are often imposed on particle geometric features (e.g. random arrangements of monodisperse or bidisperse spherical particles), the analyzed range of porosity (0.5–0.65) and consequently the order of magnitude of the predicted effective properties (e.g. permeability) which remains approximately the same across the entire dataset. Also, to the best of our knowledge, existing studies focus solely on (i) longitudinal or diagonal components of the effective tensors or (ii) applications at a fixed Péclet number. Approaches that can accurately predict the full permeability and dispersion tensors under different dynamic conditions are still lacking.

While there is no *a priori* known intrinsic limitation to the complexity of systems modeled through CNN, the cost of training, which can be significant (hundreds or thousands full pore-scale simulations) for a CNN with applicability limited to only a narrow set of idealized systems (e.g. spherical particles) and property values (e.g. limited ranges of porosities, permeabilities, etc.), there is an ongoing need to explore more efficient strategies for generating training data to encompass arbitrary morphologies and flow rates and train CNN which are more robust (i.e. retain performance) across the parameter space. This is especially critical for porous media which are generally characterized by grains with complex morphologies, have effective properties that can span many orders of magnitude (for example permeability of geologic media can easily span eight orders of magnitude), and exhibit a full range of porosity values and anisotropy ratios, while being subjected to a variety of transport dynamics ranging from diffusion- to advection-driven.

Multiscale modeling techniques, such as homogenization, offer a valuable framework to address the computational challenges associated with characterization of porous media with periodic structures (Auriault and Adler, 1995; Battiato et al., 2019; Marušić-Paloka and Piatnitski, 2005; Mikelic et al., 2006; Wall, 2007), and, as a result, they intrinsically enable the capability (i) to expand significantly the training set beyond idealistic geometries, (ii) to span a much broader parameter space in terms of porosity, permeability and dispersion coefficients, and (iii) to investigate variable transport regimes, without compromising on computational costs. In homogenization theory, the calculation of effective parameters is based on the solution of a partial differential equation (PDE), also referred to as closure problem, defined locally on a repeating unit cell, of characteristic size $\ell = \varepsilon L$ with L the macroscopic domain size and $\varepsilon \ll 1$ (Battiato et al., 2019). This approach provides a computationally efficient method for calculating permeability and dispersion in porous media, under the hypothesis that the medium can be conceptualized as being composed by periodic unit cells. Although the theoretical formalism is based on the hypothesis that the porous medium is constructed by a repetition of periodic unit cells, spatially periodic representations of porous media are routinely used to derive macroscopic properties and effective models of phenomena taking place in disordered media that lack such periodicity (Nitsche and Brenner, 1989, e.g.).

Mianroodi et al. (2022) and Weber et al. (2022) have proposed to augment CNN capabilities by taking advantage of the homogenization framework for periodic microstructures to significantly reduce the computational cost of training, while expanding significantly the size of the training set, and applied this approach to accurately predict effective diffusivity, i.e. mass transport in absence of advection, of porous structures. Previous works, including the one from Weber et al. (2022), showed that such idealizations are still representative for random systems that lack local periodicity. Following Weber et al. (2022), here we use a homogenization-informed CNN framework to predicting the full effective dispersion and permeability tensors that describe momentum and mass transport in porous media. We achieve this by generating a large training dataset of 10,000 randomly-generated images of unit cells of porous media with very diverse morphological characteristics, spanning a large range of porosities, specific surface areas and, consequently, effective parameters. The closure problems derived via homogenization to calculate permeability and dispersion are solved on each image while enforcing all global constraints imposed by homogenization theory (Ling and Battiato, 2020; Weber et al., 2024). Notably, by significantly reducing the computational cost per image, the homogenization-based approach allows us to expand the training set by orders of magnitude compared to state-of-the art datasets in the field, and to determine the full permeability and dispersion tensors for all 10,000 images in terms of varying flow rates, spanning Péclet numbers between 0 and 2000, while keeping a fixed Schmidt number that ensures Reynolds number remains in the creeping regime even at maximum Péclet. This capability enables the investigation of porous media behavior under extreme flow conditions, offering valuable insights for a wide range of applications and dynamical behaviors.

This paper is structured as follows. Section 2 provides an overview of the homogenization method used in this study, including the closure problem for calculating effective parameters. Section 3 details the generation and analysis of the training dataset, as well as the architecture of the CNN. Section 4 presents the results obtained from the proposed approach, demonstrating the accuracy and efficiency of the CNN model in predicting permeability and dispersion. Section 5 presents concluding remarks.

2. Homogenization and closure problem

This section provides an overview the macroscopic equations and boundary value problems that arise through the homogenization procedure for flow and mass transport through porous media. For details on the derivation, readers are referred to the works by, e.g., Battiato and

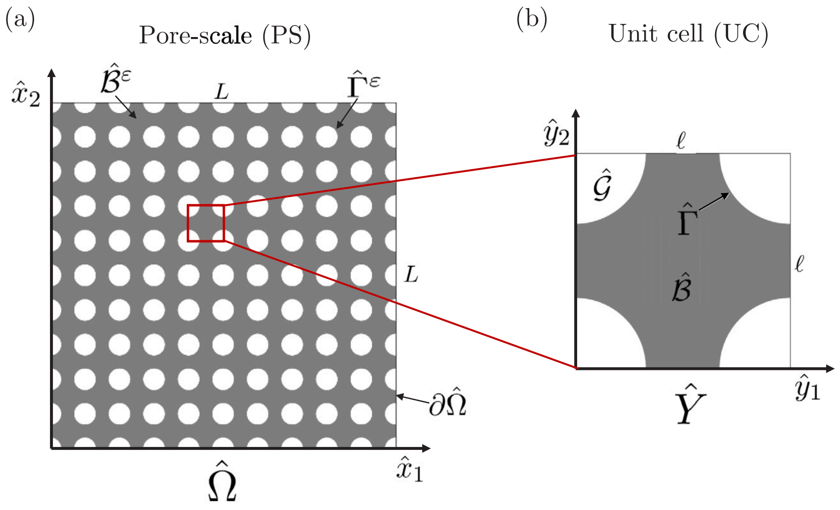

Fig. 1. Pore-scale domain (a) and unit cell (b), where $\hat{\mathbf{x}}$ and $\hat{\mathbf{y}}$ are the macroscopic and microscopic coordinate systems, respectively. The gray region indicates the fluid domain, and the white areas are grains.

Tartakovsky (2011), Boso and Battiato (2013), Pietrzyk et al. (2021) and Pietrzyk and Battiato (2023).

Consider the flow of an incompressible Newtonian fluid and solute transport in a periodic porous medium denoted as $\hat{\Omega}$ with a boundary $\partial\hat{\Omega}$ and a characteristic length L, as shown in Fig. 1(a). Homogenization theory assumes that the medium can be represented by spatially periodic unit cells denoted as $\hat{Y}$ with a characteristic length ℓ, as illustrated in Fig. 1(b). These unit cells consist of the pore space $\hat{\mathcal{B}}$ and the impermeable solid matrix $\hat{\mathcal{G}}$ separated by the smooth surface $\hat{\Gamma}$. The geometry is defined in a Cartesian coordinate system $\hat{\mathbf{x}} = (\hat{x}_1, \hat{x}_2, \hat{x}_3)$, while the coordinates spanning the unit cell domain are denoted as $\hat{\mathbf{y}} = (\hat{y}_1, \hat{y}_2, \hat{y}_3)$. The ratio between the characteristic lengths of the microscopic and macroscopic domains is given by

$$\varepsilon = \frac{\ell}{L} \ll 1. \tag{1}$$

2.1. Governing equations and dimensionless formulation

The flow field of a single-phase incompressible fluid in the interconnected pore space across all unit cells, $\hat{\mathcal{B}}^\varepsilon$, is described by the Stokes (i.e. $Re \ll 1$, where Re is the Reynolds number) and continuity equations, subject to the no-slip boundary condition at the fluid–solid interface $\hat{\Gamma}^\varepsilon$:

$$\mu\hat{\nabla}^2\hat{\mathbf{u}}_\varepsilon - \hat{\nabla}\hat{p}_\varepsilon = \mathbf{0}, \quad \hat{\mathbf{x}} \in \hat{\mathcal{B}}^\varepsilon, \tag{2}$$

$$\hat{\nabla}\cdot\hat{\mathbf{u}}_\varepsilon = 0, \quad \hat{\mathbf{x}} \in \hat{\mathcal{B}}^\varepsilon, \tag{3}$$

$$\hat{\mathbf{u}}_\varepsilon = \mathbf{0}, \quad \hat{\mathbf{x}} \in \hat{\Gamma}^\varepsilon, \tag{4}$$

where μ is the fluid dynamic viscosity and $\hat{p}_\varepsilon$ is the pore-scale pressure. The transport of a dissolved species $\mathcal{M}$ in the pore space $\hat{\mathcal{B}}^\varepsilon$ is governed by the advection–diffusion equation:

$$\frac{\partial\hat{c}_\varepsilon}{\partial\hat{t}} + \hat{\mathbf{u}}_\varepsilon\cdot\hat{\nabla}\hat{c}_\varepsilon = \hat{\nabla}\cdot\left(\hat{\mathbf{D}}\cdot\hat{\nabla}\hat{c}_\varepsilon\right), \quad \hat{\mathbf{x}} \in \hat{\mathcal{B}}^\varepsilon, \quad \hat{t} > 0, \tag{5}$$

where $\hat{\mathbf{D}}$ is the molecular diffusion coefficient which is represented as a second-order tensor for generality. Dimensionless quantities to characterize the system are introduced as:

$$\mathbf{x} = \frac{\hat{\mathbf{x}}}{L}, \quad \mathbf{y} = \frac{\hat{\mathbf{y}}}{L}, \quad \mathbf{u}_\varepsilon = \frac{\hat{\mathbf{u}}_\varepsilon}{U}, \quad \mathbf{D} = \frac{\hat{\mathbf{D}}}{D}, \quad c_\varepsilon = \frac{\hat{c}_\varepsilon}{\bar{c}}, \quad p_\varepsilon = \frac{\hat{p}\ell^2}{\mu U L}, \tag{6}$$

where U, D, and $\bar{c}$ represent characteristic values for velocity, diffusion, and concentration, respectively. Additionally, we define two time scales: $\hat{t}_D = L^2/D$ associated with diffusion and $\hat{t}_A = L/U$ associated with advection.

The Péclet number (Pe) is introduced as a dimensionless parameter defined as the ratio of the diffusion time scale to the advection time scale:

$$\mathrm{Pe} = \frac{\hat{t}_D}{\hat{t}_A} = \frac{UL}{D}. \tag{7}$$

Using the aforementioned dimensionless quantities, the previously described governing equations can be expressed in a non-dimensional form. The dimensionless version of the Stokes equations (2) is:

$$\varepsilon^2\nabla^2\mathbf{u}_\varepsilon - \nabla p_\varepsilon = \mathbf{0}, \quad x \in \mathcal{B}^\varepsilon, \tag{8a}$$

$$\nabla\cdot\mathbf{u}_\varepsilon = 0, \quad \mathbf{x} \in \mathcal{B}^\varepsilon, \tag{8b}$$

$$\mathbf{u}_\varepsilon = \mathbf{0}, \quad \mathbf{x} \in \Gamma^\varepsilon. \tag{8c}$$

Similarly, the dimensionless version of the advection–diffusion equation (5) is:

$$\frac{\partial c_\varepsilon}{\partial t} + \mathbf{u}_\varepsilon\cdot\mathrm{Pe}\nabla c_\varepsilon = \nabla\cdot\left(\mathbf{D}\cdot\nabla c_\varepsilon\right), \quad \mathbf{x} \in \mathcal{B}^\varepsilon, \quad t > 0, \tag{9}$$

where the temporal derivative has been rescaled with the diffusive time scale (i.e., $t = \hat{t}/\hat{t}_D$).

2.2. Macroscopic equations and closure problems

Here, we report a brief summary of the main steps involved in the homogenization method for completeness purposes only. More details can be found in (Auriault and Adler, 1995; Battiato and Tartakovsky, 2011; Pietrzyk et al., 2021; Pietrzyk and Battiato, 2023). Homogenization relies on the identification of two variables: a slow variable, $\mathbf{x}$, which spans the macroscopic domain, and a fast variable, $\mathbf{y}$, which spans the repeating unit cell. These variables are related by:

$$\mathbf{x} = \varepsilon\mathbf{y}, \tag{10}$$

so that spatial derivatives can be expressed as

$$\nabla = \nabla_{\mathbf{x}} + \frac{1}{\varepsilon}\nabla_{\mathbf{y}}. \tag{11}$$

First, the velocity, pressure, and concentration are expanded as integer powers of ε as follows:

$$\mathbf{u}_\varepsilon(\mathbf{x},t) := \mathbf{u}(\mathbf{x},\mathbf{y},t) = \mathbf{u}_0 + \varepsilon\mathbf{u}_1 + \varepsilon^2\mathbf{u}_2 + O(\varepsilon^3), \tag{12a}$$

$$p_\varepsilon(\mathbf{x},t) := p(\mathbf{x},\mathbf{y},t) = p_0 + \varepsilon p_1 + \varepsilon^2 p_2 + O(\varepsilon^3), \tag{12b}$$

$$c_\varepsilon(\mathbf{x},t) := c(\mathbf{x},\mathbf{y},t) = c_0 + \varepsilon c_1 + \varepsilon^2 c_2 + O(\varepsilon^3), \tag{12c}$$

and substituted into Eqs. (8) and (9). The surface and intrinsic averages $\langle\cdot\rangle$ and $\langle\cdot\rangle_{\mathcal{B}}$ are defined as:

$$\langle\cdot\rangle = \frac{1}{|Y|}\int_{\mathcal{B}} \cdot\,\mathrm{d}\mathbf{y}, \quad \langle\cdot\rangle_{\mathcal{B}} = \frac{1}{|\mathcal{B}|}\int_{\mathcal{B}} \cdot\,\mathrm{d}\mathbf{y}. \tag{13}$$

After collecting terms of like-powers of ε and obtaining a cascade of PDEs at different orders, it can be demonstrated that the macroscopic flow field is governed by Darcy's law:

$$\langle\mathbf{u}\rangle = -\mathbf{K}\cdot\nabla p_0, \qquad \nabla\cdot\langle\mathbf{u}\rangle = 0, \qquad \mathbf{x}\in\Omega, \tag{14}$$

where p_0 is a function of $\mathbf{x}$ alone (Auriault and Adler, 1995), and $\mathbf{K}$ denotes the dimensionless permeability tensor, which can be calculated as:

$$\mathbf{K} = \langle\mathbf{k}(\mathbf{y})\rangle, \tag{15}$$

where $\mathbf{k}$ and $\mathbf{a}$ are closure variables and satisfy the following boundary value problem in the unit cell

$$\nabla_{\mathbf{y}}^2\mathbf{k} + \mathbf{I} - \nabla_{\mathbf{y}}\mathbf{a} = \mathbf{0}, \quad \mathbf{y}\in\mathcal{B}, \tag{16a}$$

$$\nabla_{\mathbf{y}}\cdot\mathbf{k} = \mathbf{0}, \quad \mathbf{y}\in\mathcal{B}, \tag{16b}$$

subject to the boundary condition:

$$\mathbf{k} = \mathbf{0}, \quad \mathbf{y}\in\Gamma, \tag{17}$$

and the global condition $\langle\mathbf{a}\rangle = \mathbf{0}$, with $\mathbf{I}$ the identity tensor. Likewise, the upscaling of the advective-diffusion equation (9) leads to the macroscopic formulation (Auriault and Adler, 1995; Pietrzyk et al., 2021; Pietrzyk and Battiato, 2023):

$$\phi\frac{\partial\langle c\rangle_{\mathcal{B}}}{\partial t} = \nabla\cdot\left(\mathbf{D}^*\cdot\nabla\langle c\rangle_{\mathcal{B}} - \mathrm{Pe}\langle c\rangle_{\mathcal{B}}\langle\mathbf{u}\rangle\right), \tag{18}$$

when appropriate constraints on the magnitude of Pe number are satisfied. In Eq. (18), ϕ is the porosity and $\mathbf{D}^*$ is the effective dispersion tensor, which can be calculated as

$$\mathbf{D}^* = \langle\mathbf{D}\cdot\left(\mathbf{I}+\nabla_{\mathbf{y}}\chi\right)\rangle + \varepsilon\mathrm{Pe}\langle\chi\mathbf{k}\rangle\cdot\nabla_{\mathbf{x}}p_0. \tag{19}$$

The closure variable χ exhibits periodicity with respect to $\mathbf{y}$ and is computed as the solution to the boundary value problem:

$$-\nabla_{\mathbf{y}}\cdot\mathbf{D}\cdot\left(\mathbf{I}+\nabla_{\mathbf{y}}\chi\right) + \varepsilon\mathrm{Pe}\mathbf{u}_0\cdot\nabla_{\mathbf{y}}\chi = \varepsilon\mathrm{Pe}\left(\langle\mathbf{u}_0\rangle_{\mathcal{B}} - \mathbf{u}_0\right), \quad \mathbf{y}\in\mathcal{B}, \tag{20a}$$

$$-\mathbf{n}\cdot\mathbf{D}\cdot\left(\mathbf{I}+\nabla_{\mathbf{y}}\chi\right) = 0, \quad \mathbf{y}\in\Gamma, \tag{20b}$$

where $\mathbf{u}_0 = -\mathbf{k}\cdot\nabla_{\mathbf{x}}p_0$ and p_0 is the solution of (14). Also, $\langle\chi\rangle = \mathbf{0}$. It is important to emphasize that for the model described by Eqs. (18)–(20) to be valid, the following conditions must be satisfied (Auriault and Adler, 1995; Battiato and Tartakovsky, 2011):

$$\varepsilon \ll 1, \tag{21a}$$

$$\mathrm{Pe} < \varepsilon^{-2}, \tag{21b}$$

$$\langle\chi\rangle = 0. \tag{21c}$$

Beside the original references, the importance of these conditions and their generalizability to mildly reactive transport scenarios is also amply discussed in Weber et al. (2024, Section 2).

To summarize, homogenization theory allows one to derive both the macroscopic equations as well as their effective parameters. Such parameters, i.e. the permeability and dispersion tensors, can be determined from the closure variables $\mathbf{k}$ and χ (Eqs. (15) and (19)) which satisfy two boundary value problems in the unit cell, namely Eqs. (16) and (20). A step-by-step description of the calculation procedure can be found in Weber et al. (2024). Importantly, within this framework, the calculation of the effective parameters does not require the solution of the pore-scale problem for flow and transport at the macroscale. Finally, we note that the solution of the dispersion closure problem, Eq. (20), requires the solution of the permeability closure problem, Eq. (16), and thus we examine both in this work.

3. Methodology

This section details the generation of the training data including image generation and effective parameter calculation, as well as an overview of the CNN techniques used in this work. Although the proposed approach is applicable to both 2D and 3D structures, here we focus on 2D periodic structures to offer a proof of principle demonstration. Also, because significant differences exist between effective properties in 2D and 3D structures (Marafini et al., 2020), CNNs trained on 2D unit cells may not be used to predict properties for 3D structures.

3.1. Dataset generation and analysis

To obtain a large enough dataset to investigate the relationship between pore structure and effective transport properties (i.e. permeability and dispersion tensors) reflective of realistic and diverse porous media samples, we employ an algorithmic approach to generate synthetic samples with modifiable characteristics. While natural geological formations exhibit significant variability, it can be challenging to acquire a sufficiently large dataset encompassing a wide range of topological characteristics such as porosity, specific surface area, pore size distribution, and tortuosity, among others. Briefly, the method consists in placing a random number of randomly shaped particles onto an empty canvas until a stopping criteria is reached. The placement, size, and orientation of these particles are determined from statistical distributions and rules motivated by observation.

Using the aforementioned algorithm, we generate 10,000 binary two-dimensional 224 × 224 pixel images. Next, various morphological properties such as porosity, specific surface area, and connectivity are computed for each image. Fig. 2(a) shows a scatter plot displaying the porosity and specific surface area of each image in the dataset with the color of each datapoint depicting the number of particles in the unit cell. Fig. 2(a) shows that the dataset spans porosity values between 0.25 and 0.85, a (solid particles) perimeter range of 3.5ℓ to 10.5ℓ, with ℓ the length of the unit cell, and images containing 3–25 particles. To provide a visual representation of the dataset, Fig. 2(b) displays 25 example images organized by their topological characteristics and showcases the broad range and quality of the dataset used in this work, demonstrating the diversity and complexity of the synthetic porous media samples generated.

3.2. Permeability

Next, we compute the permeability tensor for each image in the dataset by solving the closure problem described in Section 2, Eq. (16). We follow the algorithm described by Ling and Battiato (2020) and Weber et al. (2024), to enforce global constraints on all closure variables while converging to a unique solution, as shown in the aforementioned references. We use the open-source computational fluid dynamics (CFD) software OpenFOAM to perform the meshing and compute the solution of (16). Fig. 3 presents a scatter plot showing the diagonal components, $K_{11} = [\mathbf{K}]_{11}$ and $K_{22} = [\mathbf{K}]_{22}$, of the calculated permeability tensor which span four orders of magnitude in both directions, with the smallest dimensionless permeability in the order of 10^{-6} and the largest in the order of 10^{-2}. The dataset includes highly anisotropic samples, where the permeability components differ significantly along different directions with the ratio K_{11}/K_{22} ranging between 10^{-2} and 10^{2}. Furthermore, the off-diagonal terms of the permeability tensors indicate the presence of cross-coupling between flow directions, which arises from the specific connectivity of pores and channels within the pore-scale structures. By capturing this diverse range of structures and properties, our dataset provides a comprehensive representation of porous media structures encountered in a variety of systems.

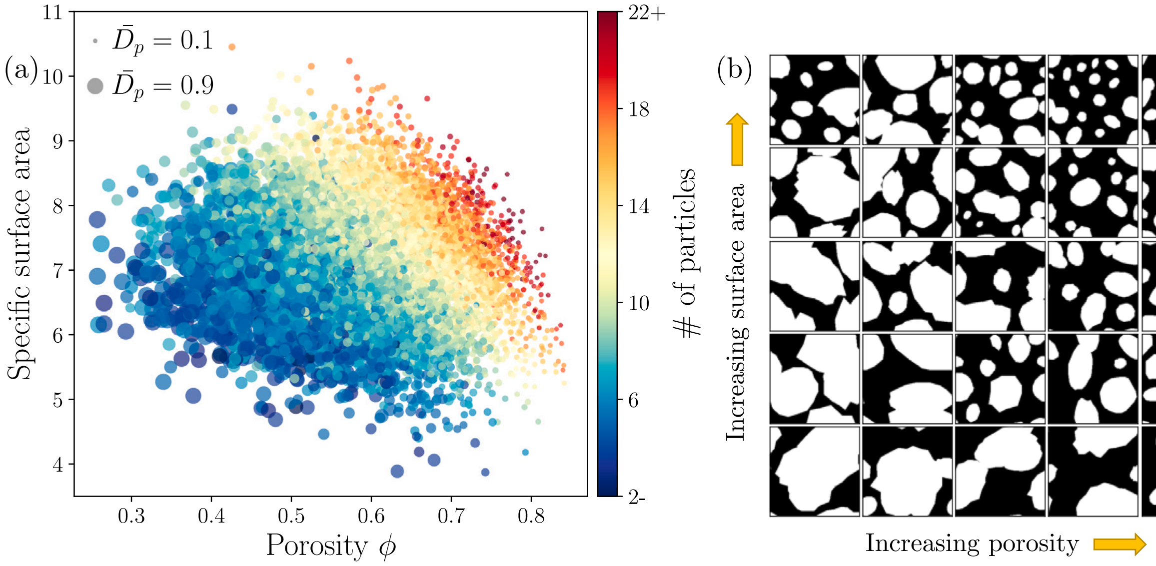

Fig. 2. (a) Scatter plot depicting porosity and specific surface area – normalized by the side length of the unit cell – for each of the 10,000 images generated. The color coding represents the number of particles in the unit cell while the size of the datapoint corresponds to the average particle diameter in the unit cell. (b) Example images from the dataset showing the broad range of morphologies considered.

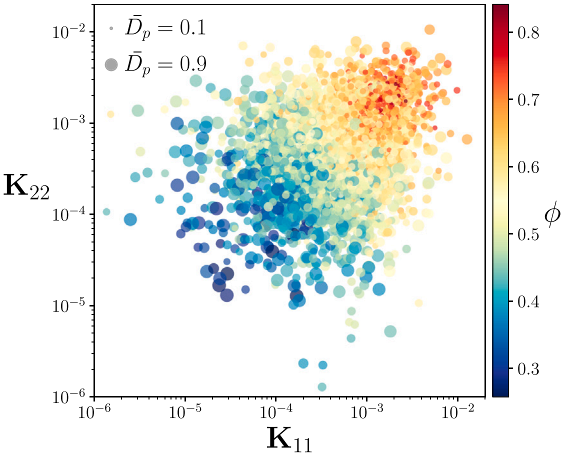

Fig. 3. Scatter plot depicting the K_{11} and K_{22} coefficients for each image in the dataset. The color of each datapoint represents the porosity of the sample image. The plot indicates that the dataset includes a large variety of structures with different level of anisotropy.

3.3. Dispersion

After solving the closure problem to determine permeability, we compute the effective dispersion tensor for each image sample for nine values of Péclet number between 0 and 2000. This is achieved by solving the dispersion closure problem described in Section 2, Eq. (20). While below we provide a brief outline of the method, we refer the reader to Weber et al. (2024) for a step-by-step description of the algorithm for the solution of the dispersion closure problem (20). We emphasize that for a given Pe number, $\nabla_{\mathbf{x}} p_0$ must be chosen consistently as discussed in Weber et al. (2024, Section 3). For any given Pe number, a pressure gradient $\nabla_{\mathbf{x}} p_0 = [\nabla_{x_1} p_0, \quad 0]$ in the x_1 direction is imposed such that the characteristic velocity is $U := \langle \hat{\mathbf{u}} \rangle_{\mathcal{B}}$, or alternatively

$$\langle \mathbf{u} \rangle_{\mathcal{B}} = 1. \tag{22}$$

This ensures that for each image, $\mathbf{k}$, ∇p_0, $\mathbf{u}_0$ and $\langle \mathbf{u}_0 \rangle_{\mathcal{B}}$ are fixed, while Pe can be independently changed in Eq. (20) to account for the impact of different transport regimes on the effective dispersion tensor.

Since the flow is driven for each image in the x_1-direction, the D^*_{11} component increases most rapidly with Pe and spans the broadest range of values (nearly four orders of magnitude). In all simulations, ϵ, the separation of scale parameter defined in Eq. (1), is set to 0.02 and each image is solved for $\text{Pe} = \{0, 10, 20, 50, 100, 200, 500, 1000, 2000\}$. This corresponds to a total of 100,000 simulations for the solution of the permeability and dispersion tensors combined, and enable us to explore a significantly wider range in the parameter space compared to previous studies, while ensuring that the applicability conditions of the homogenized model are not violated (Pietrzyk et al., 2021) and the flow remains creeping. This is achieved by prescribing a fixed Schmidt number $\text{Sc} = \nu/D = 10^3$, a value typical for many solute–solvent systems. This ensures that as Pe increases, the Reynolds number remains small, and the flow stays within the creeping regime.

Fig. 4 displays each component of the effective dispersion tensor for the dataset, illustrating that the relationship between Péclet number and the dispersion tensor components is highly dependent on the image microstructure. The color of each line represents the porosity of the individual sample. This figure demonstrates why empirical relationships that assume a given functional form between dispersion coefficient and Péclet can lead to large inaccuracies depending on the specific microstructure morphology. It is worth emphasizing that the off-diagonal components of the dispersion tensor associated with certain images may swap sign from positive to negative (or vice-versa) with increasing Pe: this implies that different cross-directional pathways become preferential under different flow regimes. This highlights the importance of appropriate quantification of the effective dispersion using pore-scale simulations or closure formulations to maintain computational efficiency and predictive accuracy. As displayed in Fig. 4, our image dataset showcases a comprehensive representation of dispersive behaviors. By including a wide range of flow conditions and both diagonal and off-diagonal components of the dispersion tensor, our dataset enables a thorough investigation of the relationship between pore structure and effective properties.

While Fig. 4 demonstrates the range of the dataset, it does not illustrate how the characteristics of each individual image impact the dispersion tensor. To investigate more closely and provide tangible examples of the impact of microstructure on the effective dispersion tensor, we select six images that represent different dynamic scenarios. These examples were chosen to illustrate diverse geometric and transport scenarios as a preliminary investigation. Additional discussion is

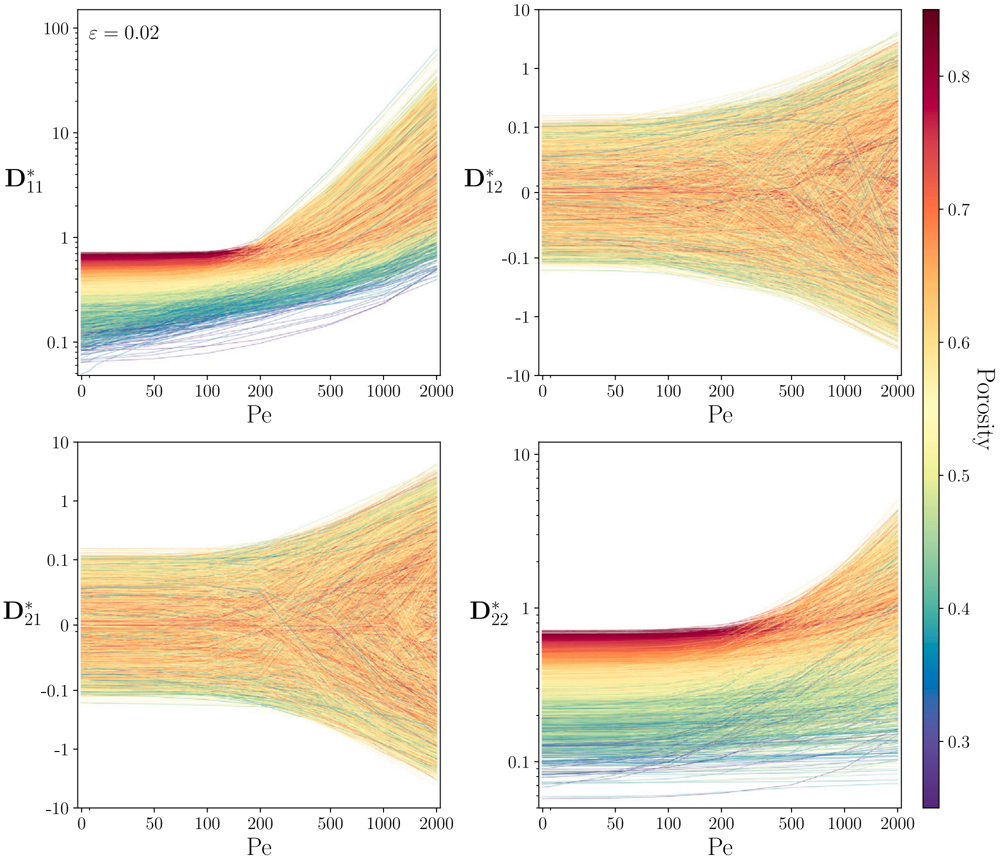

Fig. 4. Plot depicting all components of the effective dispersion tensor for each of the 10,000 images of the dataset. Each line represents the component of the dispersion tensor associated to one specific unit cell image in terms of Péclet number. The color of each line denotes the porosity of the given sample. Note the y-axes for the off-diagonal coefficients are *semi-logarithmic*, meaning it is log scale except in the interval between −0.1 and 0.1, where the scale is linear.

provided in Appendix. The six images are presented in Fig. 5(right) and are arranged from highest porosity (Ex. 1) to lowest porosity (Ex. 6). The pore-space colorization in Fig. 5(left) depicts the local velocity field determined by $\mathbf{u}_0 = -\mathbf{k} \cdot \nabla_{\mathbf{x}} p_0$, where $\mathbf{k}$ is determined through the permeability closure problem, Eq. (16). In each unit cell, $\nabla_{\mathbf{x}} p_0$ is defined to be nonzero only in the x_1 (horizontal) direction. Thus, while flow can occur in the vertical direction due to interactions with particles, the pressure gradient in each case propels the flow from left to right. The effective dispersion tensors for each of the considered images are presented in Fig. 5(right) for Pe = 0 through Pe = 2000.

The first notable observation in Fig. 5 is the impact of porosity. Higher porosity images tend to exhibit higher effective diagonal components of the dispersion tensor at Pe = 0, i.e. higher effective diffusivities D^*_{11} (Pe = 0) and D^*_{22} (Pe = 0). The same trend is apparent also in Fig. 4, where the color of the lines corresponds to the image porosity. Additionally, in Fig. 5, higher porosity images tend to have smaller magnitudes of off-diagonal coefficients, $D^*_{12} = [\mathbf{D}^*]_{12}$ and $D^*_{21} = [\mathbf{D}^*]_{21}$, which represent cross-flow characteristics, particularly at low Pe. Positive values of these coefficients indicate that concentration moving in the positive y_1 (right) direction in the unit cell is redirected upwards in the positive y_2 (up) direction, while negative values of off-diagonal coefficients indicate downward redirection (Dejam and Hassanzadeh, 2022). Due to the reduced presence of solid particles in high porosity images, solute advecting from left to right can traverse the unit cell with minimal vertical transport. Hence, it is expected that high porosity images have the smallest magnitudes of D^*_{12} and D^*_{21}. This can also be seen in Fig. 5, where Ex. 1, 2 and 3 show near-zero values for the initial off-diagonal components.

Another feature worth highlighting is the relationship between the components of the effective dispersion tensor and Pe for each image. While each example exhibits its own unique functional dependence between the components of the dispersion tensor and Pe, a noticeable trend emerges in images which contain a distinct horizontal flow channel, such as Ex. 3 and Ex. 6. In these instances, the majority of flow (and consequently solute mass transport) occurs within these channels. Since the characteristic velocity used to calculate Péclet number, $\langle \mathbf{u} \rangle_B$, is averaged over the entire pore-space (Eq. (7)), these channels experience a much higher local Pe compared to the unit cell as a whole. Therefore, as Pe increases, D^*_{11} experiences a much more rapid increase in terms of Pe number compared to other topologies, as the solute is increasingly and efficiently transmitted in the horizontal direction along these localized flow paths. The same principle applies to vertically-oriented flow channels. This is best represented by Ex. 4. In this case, the specific pore-scale solid particles' orientation creates a tortuous pathway that greatly restricts transport in the y_1-direction, resulting in increased mass transport in the vertical y_2-direction as Pe increases. The D^*_{22} component reflects this behavior, as it significantly increases with higher Pe. Since this vertical transport is in the positive y_2-direction, the off-diagonal components increase substantially in a positive direction as well.

In the following Sections 3.4 and 3.5, we present the CNN architecture and the data augmentation procedure, respectively.

3.4. CNN architecture

CNNs have proven to be effective in predicting properties from images due to their ability to capture spatial patterns and hierarchies of features. Each convolutional layer applies localized filters that scan across the input to detect geometric patterns, from simple edges to complex structures. As shown in Table 1, deeper layers reduce spatial resolution while increasing the number of channels, allowing the

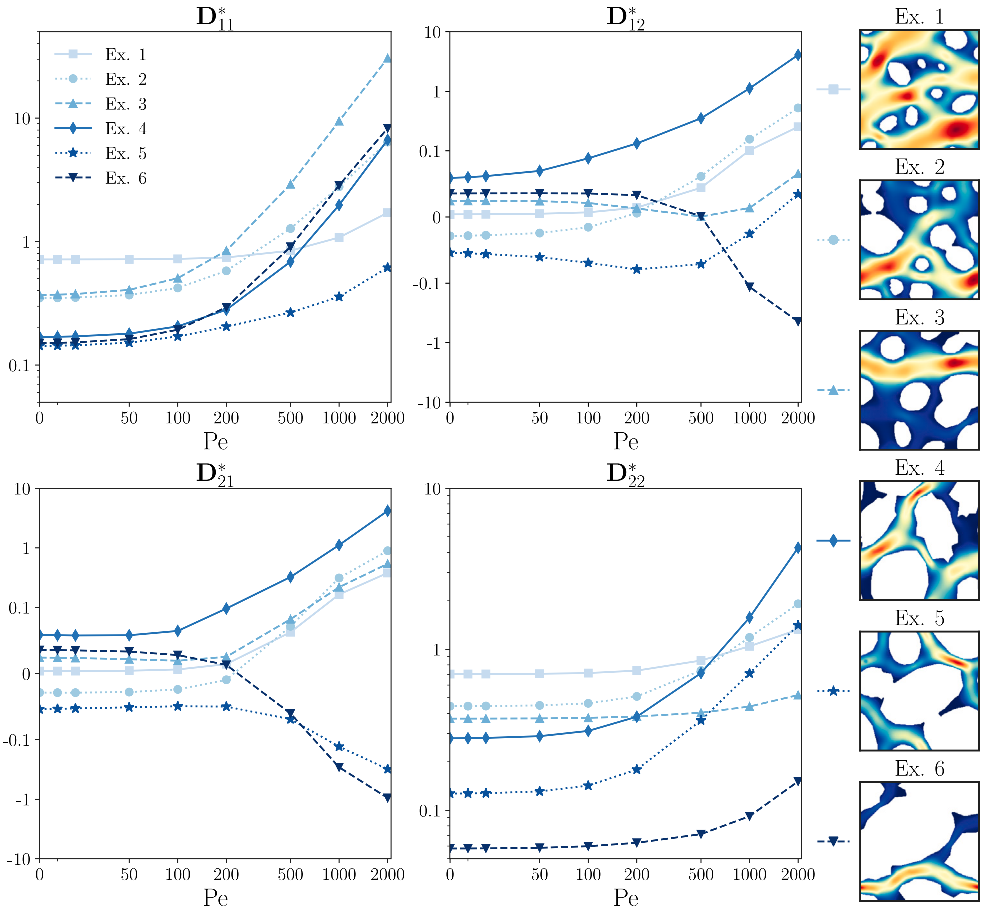

Fig. 5. The effective dispersion tensors for the example images considered. (Right) 6 example images of the dataset. The white represents solid particles, and the coloring in the pore space reflects the magnitude of the velocity field $\mathbf{u}_0 = -\mathbf{k}\nabla_\mathbf{x} p_0$ with $\mathbf{k}$ derived from the permeability closure problem and $\nabla_\mathbf{x} p_0$ defined nonzero only in the x_1 (horizontal) direction. Note the y-axes for the off-diagonal coefficients are *semi-logarithmic*, meaning it is log scale except in the interval between -0.1 and 0.1, where the scale is linear.

network to build progressively richer representations of the porous geometry. In this study, we employ a CNN to predict both permeability and effective dispersion tensors from the 224×224 pixel binary images discussed previously. The training process involves optimizing the network parameters using the ADAM optimization algorithm implemented in PyTorch (Kingma and Ba, 2015). Batch normalization on the activations between convolutional layers is used to improve training (Ioffe and Szegedy, 2015), and dropout is incorporated in the fully connected layers to prevent overfitting (Srivastava et al., 2014). Additionally, input normalization is performed to ensure consistent scaling across the dataset by setting binary input images to contain values of -1 or 1 and normalizing all other inputs to have zero-mean and unit-variance. To promote Galilean invariance during training, we randomly shifted each input image in both horizontal and vertical directions at every epoch (with periodic wrapping), so the model learned to associate different periodic realizations of the same microstructure with the same effective transport tensors.

We employ two CNNs to predict permeability by dividing the task into diagonal and off-diagonal components. This approach takes advantage of the rotational symmetry of the permeability tensor. When an image is rotated by 90°, the corresponding tensor transforms from $\left[K_{11}, K_{12}; K_{21}, K_{22}\right]$ to $\left[K_{22}, -K_{21}; -K_{12}, K_{11}\right]$. Hence, we can train a CNN to predict K_{11} and then rotate the image to predict K_{22}. The same principle applies to the off-diagonal components with a negative sign. By adopting this approach, we effectively double the training data size for permeability. In the next subsection, we will elaborate on how we further augment this data through flipping.

For dispersion prediction, we design a CNN architecture which is divided into four parallel branches, one for each component of the dispersion tensor. These four branches can be thought of as independent CNNs for estimating each tensorial component. To capture the different behaviors across the wide Pe range of the dataset, each component branch of the dispersion CNN is further divided into low Péclet ($\text{Pe} < 20$), mid Péclet ($20 < \text{Pe} < 200$), and high Péclet ($200 < \text{Pe} \leq 2000$) regions. This allows the CNN to refine predictions for different regimes where the preferential flow channels may change as Pe number is increased. This architecture is illustrated in Fig. 6, and details of the layer size parameters for a given component are shown in Table 1.

In addition to the binary image input, we explore the inclusion of various transformations of the input data to improve prediction accuracy. One such transformation is the “distance map”, which calculates the Euclidean distance to the nearest surface for each location in the pore space. Another transformation is the “opening map”, which identifies the largest pore openings in the image. Each transformation is calculated using the software from Boelens and Tchelepi (2021), and examples of the computed transformations are shown alongside the input in Fig. 6. These additional input features provide complementary information about the pore structure and we turn them on and off for various networks to understand how their inclusion impacts CNN performance.

We adopt a cosine learning rate schedule which decreases the learning rate during each epoch of training, promoting better convergence. To determine the optimal initial learning rate and weight decay, we conduct hyperparameter tuning using the development set to achieve the best performance and find that an initial learning rate of $\alpha = 10^{-3}$ and a weight decay of $\lambda = 10^{-8}$ works best for each case. During the training process, we employ a smooth L1 loss function to minimize the difference between predicted and desired output values. The performance of the CNN models is quantified using the Root Mean

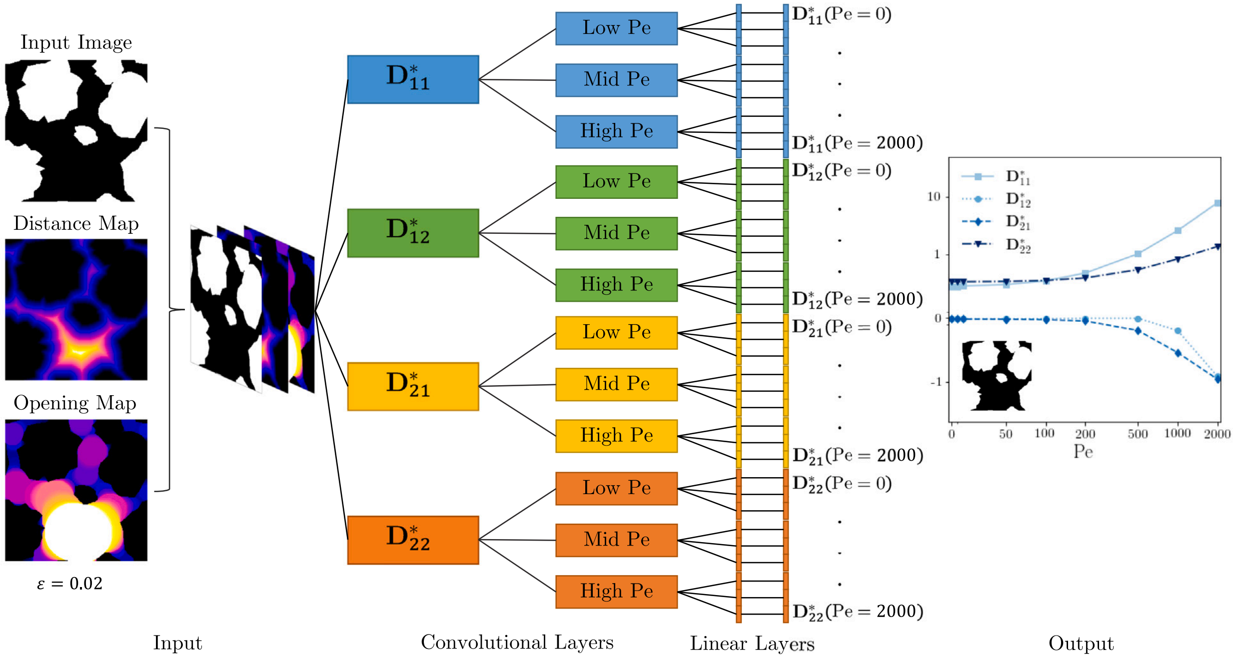

Fig. 6. Diagram of the proposed CNN for dispersion prediction. The CNN takes a binary image as an input, makes the desired transformations, then branches into predicting the full dispersion tensor for Pe = 0 through Pe = 2000.

Square (RMS) error metric, which provides a measure of the overall prediction accuracy. The training is performed for 100 epochs, and the final CNN selected is that which performed best on the development set — not necessarily the final epoch.

3.5. Data augmentation

We first split the dataset into a training set of 9000 images, development set of 500 images, and validation set of 500 images. To increase the dataset size, we augment the data with flipped transforms of the original images–though each image transform stays in the same set as the original image so that the sets remained completely independent of each other. All permeability and dispersion tensors are computed once for each original via the closure problems described in Section 2, and no simulations are performed on the transformed images. For permeability prediction, we leverage the symmetry properties to generate additional training examples. By flipping the image along either the x_1 or x_2 direction, the permeability tensor is transformed from $[K_{11}, K_{12}; K_{21}, K_{22}]$ to $[K_{11}, -K_{12}; -K_{21}, K_{22}]$. In the dispersion case, the same relationship holds for the diagonal components D^*_{11} and D^*_{22}. For the off-diagonal components, D^*_{12} and D^*_{21}, flow reversal symmetry holds in the x_2 (vertical) direction, but not along the x_1 (horizontal), particularly for high Pe, as discussed by Pride et al. (2017). This data augmentation process with flipped counterparts effectively quadruples the dataset size for both permeability and diagonal dispersion components while doubling the dataset size for off-diagonal dispersion predictions. Note that the transformed image is passed through the CNN, and the corresponding transformed output tensor is compared to the known label from the original image with the appropriate sign or index permutation applied. Additionally, inputting flipped images through the CNN at test time and averaging the predicted quantities, we guarantee that the CNN output maintains the same symmetry properties of the original data. In other words, inputting a flipped image through the CNN will result in the same output tensor with the desired transformation consistent with physical behavior. The data augmentation process leads to the expansion of the original dataset from 10,000 images to 80,000 images for permeability (taking additionally into account the rotation discussed in the previous subsection), 40,000 images for diagonal dispersion coefficients, and 20,000 images for off-diagonal dispersion coefficients. One other benefit of this data augmentation process is that it guarantees physical consistency, as rotating an image 90° would result in swapping the diagonal coefficients at the prediction stage.

4. Results and discussion

4.1. Permeability

To investigate the impact of additional input transformations, namely the opening map and distance map discussed in Section 3, we trained CNN models with and without these transformations. Table 2 summarizes the results for each CNN. The results show that incorporating both transformations slightly improves the permeability predictions. The opening map displays information about the positions of the largest pores in the image, while the distance map captures the proximity to solid particles at each point in the pore space to give the CNN complementary features. Fig. 7 shows the validation set results for the model which included both transforms as inputs. As seen in both Fig. 7 and Table 2, we present the permeability prediction into two groups, diagonal and off-diagonal components. This is because the permeability coefficient depends on geometry alone and is independent of a flow condition or direction, i.e. predicting K_{11} is equivalent to predicting K_{22} for a rotated image, and thus they can be combined together accordingly. To evaluate the error, we use a percentage-based RMS approach that normalizes residuals by the average magnitude of the data for each ij component of the tensor:

$$\mathrm{RMS}_{\%,ij} = \left[\frac{100}{N} \sum_{k=1}^{N} \left(\frac{\hat{K}_{ij} - K_{ij}}{K_{ij}} \right)^2 \right]^{0.5} \tag{23}$$

where N is the number of samples in the validation set and $\hat{\cdot}$ denotes the prediction. Reported $\mathrm{RMS}_{\%}$ values are sensitive to small true values, particularly for off-diagonal terms, which are often orders of magnitude smaller than their diagonal counterparts and can be negative. For diagonal components, the CNN significantly outperforms Kozeny–Carman model, while also providing predictions for off-diagonal terms that such models cannot address. The CNN achieves high accuracy across a range

Table 1
Details of each layer in the dispersion prediction CNN and its output dimensions. The input is a $c \times 224 \times 224$ image, where c = (1, 2, or 3) depending on the inclusion of transformation maps. W denotes the convolutional filter width, s is the stride (step size), and p is the amount of periodic padding. The "groups" parameter indicates how many independent parallel branches are used in the convolution; these branches process the input separately and do not merge, as shown in Fig. 6. The final output of each independent network is a single tensor component.

No.	Layer	Size
0	Input	$c \times 224 \times 224$
1	Convolution ($W = 11$, $s = 1$, $p = 5$, groups = 4) Leaky ReLU, BN	$12 \times 224 \times 224$
2	Convolution ($W = 9$, $s = 2$, $p = 4$, groups = 4) Leaky ReLU, BN	$12 \times 112 \times 112$
3	Convolution ($W = 7$, $s = 2$, $p = 3$, groups = 4) Leaky ReLU, BN	$16 \times 56 \times 56$
4	Convolution ($W = 7$, $s = 2$, $p = 3$, groups = 4) Leaky ReLU, BN	$96 \times 27 \times 27$
5	Convolution ($W = 7$, $s = 2$, $p = 3$, groups = 12) Leaky ReLU, BN	$192 \times 13 \times 13$
6	Convolution ($W = 5$, $s = 2$, $p = 1$, groups = 12) Leaky ReLU, BN	$384 \times 7 \times 7$
7	Convolution ($W = 3$, $s = 2$, $p = 1$, groups = 12) Leaky ReLU, BN	$768 \times 4 \times 4$
8	Convolution ($W = 3$, $s = 2$, $p = 1$, groups = 36) Leaky ReLU, BN	$4608 \times 2 \times 2$
9	Convolution ($W = 2$, groups = 36) Leaky ReLU, Flatten	9216×1
10	Dropout Linear (groups = 36) Leaky ReLU	3456×1
11	Dropout Linear (groups = 36)	36×1

Table 2
Comparison of the four networks with different input transformations results on the validation dataset for permeability prediction.

Index	Distance	Opening	Permeability RMS Error	
	Map	Map	$K_{11}\&K_{22}$	$K_{12}\&K_{21}$
1	No	No	13.24%	34.05%
2	Yes	No	11.36%	32.09%
3	No	Yes	12.02%	32.55%
4	Yes	Yes	10.31%	30.35%

of permeability coefficients spanning 3 orders of magnitude. To the best of our knowledge, this is the first study that not only attempts to predict permeability over such a broad range of values (three orders of magnitude), but also does so with high accuracy, while keeping computational costs in check. These results demonstrate the value of augmenting CNN approaches with formal homogenization methods, which allowed (within the rigor of the theoretical framework) the use of a vast dataset with minimal time required to generate and simulate.

To further assess the performance of the CNN models, we compare their predictions with the empirical Kozeny–Carman model, a widely used approach for estimating permeability from porosity and average particle size. The Kozeny–Carman equation is expressed as:

$$\hat{K}_{ii} = \frac{\phi^3 \bar{D}_p^2}{C(1-\phi)^2} \tag{24}$$

Table 3
Average RMS across all Pe for the four networks with different input transformations results on the validation dataset for dispersion prediction. Note that RMS for the off-diagonal components was calculated on an absolute basis and not percentage as the small magnitudes of the coefficients causes numbers to blow up.

Index	Distance	Opening	Dispersion RMS Error			
	Map	Map	D^*_{11}	D^*_{12}	D^*_{21}	D^*_{22}
1	No	No	10.07%	0.098	0.117	9.41%
2	Yes	No	9.84%	0.088	0.097	8.53%
3	No	Yes	10.00%	0.091	0.098	9.28%
4	Yes	Yes	9.73%	0.090	0.097	9.10%

where ϕ is porosity, $\bar{D}_p$ is the average particle diameter, and C is a fitting constant. Notably, the Kozeny–Carman model (i) cannot account for anisotropy as there is no directional information incorporated in the estimation of the diagonal components of the permeability tensor and (ii) does not provide an estimate for the off-diagonal terms. Nonetheless, we compare its diagonal coefficient predictions with the CNN models for each dataset image in Fig. 7 and show that the CNN vastly outperforms this empirical model. Although no explicit constraints were imposed during training, all 500 predicted permeability tensors in the test set were verified to be positive-definite (i.e. symmetric with positive eigenvalues), reflecting the model's ability to learn this physical property from the training data. Compared to the numerical solution of the closure problem for permeability, the computational speedup achieved by the trained CNN is approximately 10^5 for any given image. This substantial speedup enables rapid predictions, making the CNN approach a highly practical and scalable solution for permeability estimation.

4.2. Dispersion

The homogenization-augmented CNN approach was also applied to predict the dispersion tensor of the synthetic dataset. Similar to the permeability prediction, we utilized the opening map and distance map as additional input transformations. Table 3 presents the results of the CNN models for dispersion prediction and shows that the inclusion of the input transformations in this case does not have a very dramatic impact on prediction accuracy as all models perform very well with RMS in the order of 10%. Fig. 8 showcases the parity plot comparing each component of the dispersion tensor determined from the closure solution (x-axis) and the homogenization-augmented CNN (y-axis) for all data points in the validation set and Pe numbers ranging across three order of magnitudes between 0 and 2000. The CNN predictions presented in Fig. 8 correspond to those including both input transformations. Fig. 8 shows the overall accuracy across all Péclet numbers. We note that the predicted dispersion tensors are not strictly symmetric, which is consistent with prior findings in numerical and experiment studies that asymmetry can emerge in anisotropic porous media due to directional differences in solute spreading (Auriault et al., 2010). For the 4500 dispersion tensor predictions across the test set (9 Pe values for each of 500 images), 99.22% were found to have positive eigenvalues. This high empirical consistency suggests that the model learned this physical constraint despite it not being explicitly enforced.

Although there is a degradation in performance at the highest Péclet number due to the increasing influence of advective transport, the predictions remain fairly accurate through Pe = 2000. Fig. 9 displays the average error at each Péclet number. It can be observed that higher errors occur under the fastest flow conditions considered in this study: this is not unexpected since the onset of preferential flow paths and advective-dominated transport at high Péclet numbers becomes increasingly dependent on fine pore-scale geometric features compared to more-diffusion dominated transport, as apparent in Fig. A.12. This effect is further amplified when the range of geometric parameters at

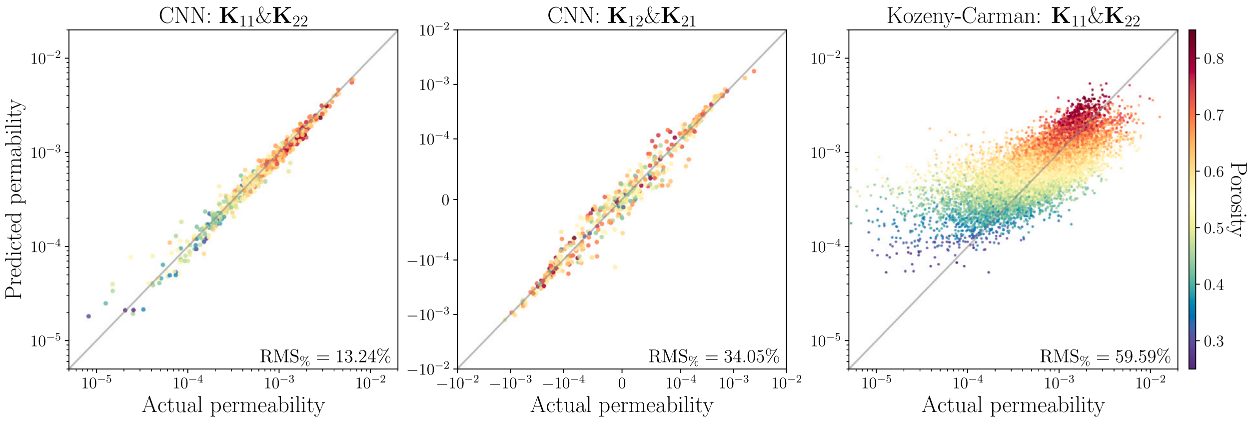

Fig. 7. CNN results for the permeability dataset for diagonal coefficients (left), off-diagonal coefficients (middle) compared with the same plot using the Kozeny–Carman equation to predict permeability (right). The color of each datapoint represents the porosity of the image. The CNN results shown here are for the network that included both the distance map and opening map transformations discussed.

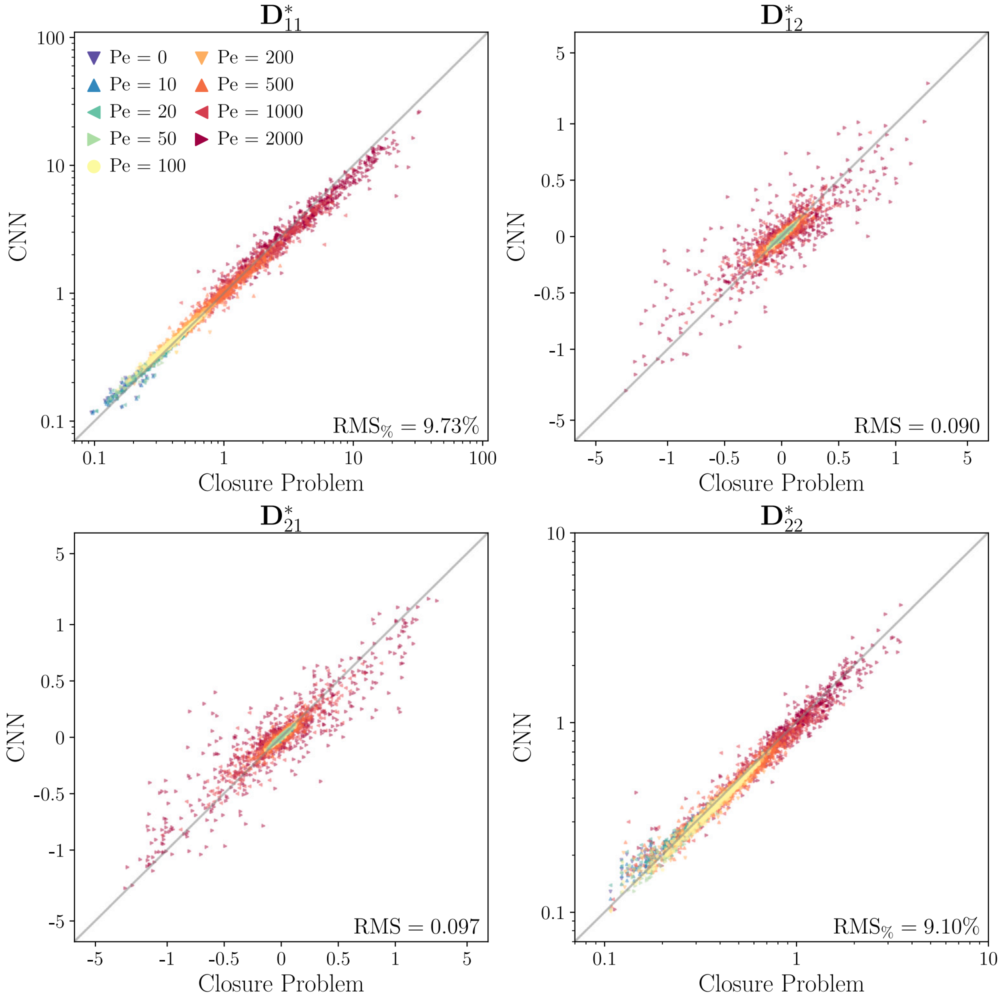

Fig. 8. CNN results on the validation set for predicting the components of the dispersion tensor for all Péclet numbers. The CNN results shown are for the network with both the distance and opening map included.

the pore-scale is as broad as the one considered in this study and spans orders of magnitude in pore-scale topologies, porosity values, specific surface area, and effective parameters. We speculate that increasing the training set size would improve the CNN performance for high Péclet numbers. It is worth emphasizing that this dynamic conditions also correspond to increased simulation time due to the need for decreasing time steps to maintain stability.

These results overall demonstrate that marrying CNN with rigorous homogenization theory (i) allows to significantly broaden the CNN model predictivity across orders of magnitude in the parameter space while not compromising on computational efficiency, (ii) enables one to capture the intricate dynamics of dispersion and (iii) holds promise for various applications that require accurate characterization of solute transport in porous media across a broad range of parameters.

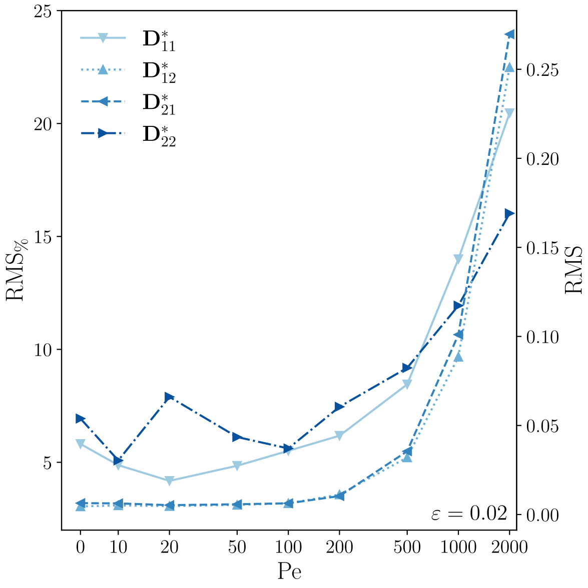

Fig. 9. Average RMS error for CNN-predicted dispersion as a function of Péclet number. Is is seen that the majority of the error occurs at $\mathrm{Pe} = 2000$ in each case.

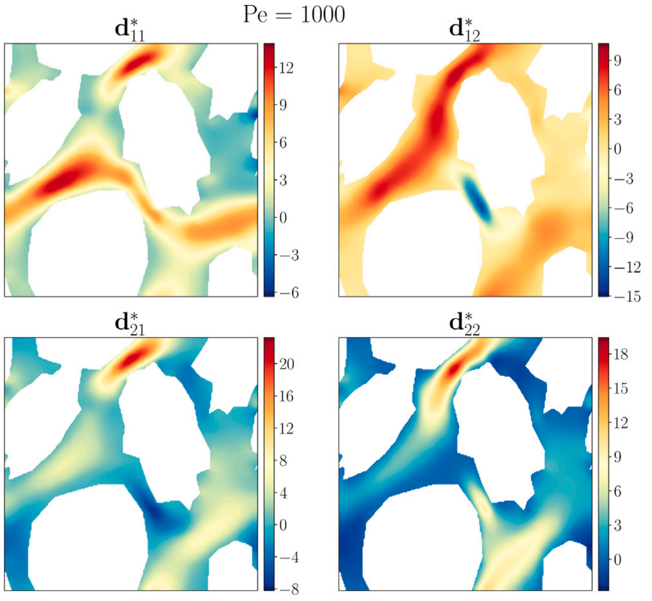

Fig. A.10. Plots depicting each component of $\mathbf{d}^*$ for Ex. 4 at $\mathrm{Pe} = 1000$. This example features a strong diagonal channel that drives flow up as it moves to the right. This channel becomes more prominent at high Pe and can be seen clearest in the $\mathbf{d}^*_{12}$ and $\mathbf{d}^*_{21}$ component plots.

5. Conclusion

In this work, we presented an approach that combines deep learning with multiscale modeling techniques to predict permeability and dispersion tensors in porous media. By leveraging the computational efficiency of homogenization theory – where effective parameters can be computed relatively quickly from a small unit cell of the periodic microstructure – and generating a large dataset of porous media images, a CNN was trained to estimate these transport properties from microstructural images and input flow conditions spanning many dynamic regimes. To the best of our knowledge, the range of geometric and dynamic parameters investigated and predicted is unprecedented and spans between 2 and 4 orders of magnitude in the diagonal components of the dispersion tensor, and nearly 3 orders of magnitude in permeability. These unique performance capabilities of the trained CNN were enabled by framing the CNN model within the homogenization framework. Homogenization theory, which is based on the hypothesis of periodic heterogeneous porous media, offers a rigorous framework to help both conceptualize and demonstrate that the issues associated with large training costs of CNNs in the context of effective parameters' predictions across orders of magnitude can be mitigated by taking advantage of the underlying properties of the microstructure. More broadly and beyond periodic structures, these results suggest that the identification of the proper size of the domain over which a closure problem will be defined and solved is an important step to control CNN training costs, enlarge the size of the overall training set and ultimately improve the performance of the CNN across topologies and dynamic conditions.

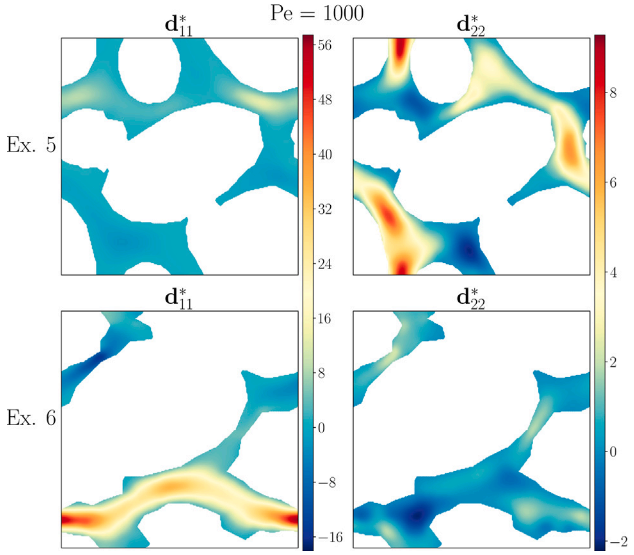

Fig. A.11. Comparison of diagonal components of $\mathbf{d}^*$ for Ex. 5 (top) and Ex. 6 (bottom) at $\mathrm{Pe} = 1000$. Ex. 6 has a horizontal flow channel which causes d^*_{11} to increase rapidly at high Pe whereas the particles in Ex. 5 cause mass transport to happen preferentially in the vertical direction, so d^*_{22} increases with high Pe.

We emphasize that, although the homogenization-augmented CNN framework was demonstrated for 2D periodic structures and incompressible and creeping flow of a Newtonian fluid with nonreactive solute transport of a single chemical species, it does not have intrinsic theoretical limitations for its application/generalization to 3D periodic structures and more complex systems, e.g. homogeneous and/or heterogeneous multispecies reactions, potentially unsteady and inertial systems and non-Newtonian fluids. The applicability of this framework only strictly (mathematically) requires the existence of a periodic unit cell (be it 2D or 3D - although homogenization theory has been demonstrated to work well also for system that lack such periodicity) and the existence of the homogenized/upscaled form for the system of interest, which includes a set of macroscopic PDEs, the closure to be solved in the unit cell, and the definition of all effective parameters as a function of closure variables. As the system complexity increases both in terms of physics and spatial dimensions, it is expected that the computational cost for training will increase. Current work involves the application of this framework to non-linear heterogeneous highly reactive solutes using the homogenized model derived in Pietrzyk and Battiato (2023). These results demonstrate the homogenization-augmented CNN's ability to quickly characterize effective properties for a wide range of images with significantly higher accuracy than more

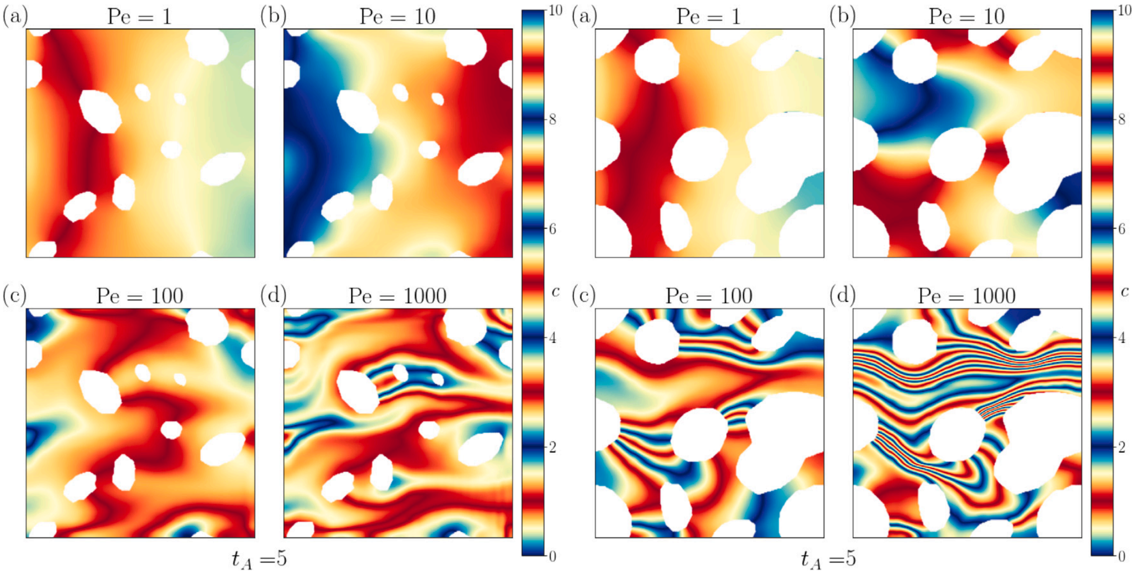

Fig. A.12. The final time step ($t_A = 5$) of the transport simulation for Ex. 1 (left four panels) and Ex. 3 (right four panels). The concentration color map is periodic to better visualize streamlines for a wide range of concentration values. It should be noted that with the periodic concentration map, a red value could indicate a concentration of $c = \{1, 3, 5, \dots\}$. (Left (a)–(d)) Ex. 1 unit cell is high porosity with particles that are evenly distributed throughout the unit cell. As such, no clear preferential flow path emerges as Pe is increased and $\mathbf{D}^*$ does not increase substantially with increasing Pe. (Right (a)–(d)) In Ex. 3, the horizontal flow channel sees increasingly more concentration at higher Pe, while limited mixing is experienced in the vertical direction. Hence, D^*_{11} increases rapidly with increasing Pe, while D^*_{22} does not.

classical empirical correlations, offering great potential for enhancing porous media characterization and prediction in diverse scientific and engineering applications.

CRediT authorship contribution statement

Ross M. Weber: Writing – original draft, Software, Methodology, Investigation, Formal analysis, Data curation, Conceptualization. **Ilenia Battiato:** Writing – review & editing, Supervision, Methodology, Funding acquisition, Conceptualization.

Declaration of competing interest

The authors declare the following financial interests/personal relationships which may be considered as potential competing interests: Ilenia Battiato reports financial support was provided by US Department of Energy Office of Science. If there are other authors, they declare that they have no known competing financial interests or personal relationships that could have appeared to influence the work reported in this paper.

Acknowledgments

This work was supported as part of the Center for Mechanistic Control of Water–Hydrocarbon–Rock Interactions in Unconventional and Tight Oil Formations (CMC-UF), an Energy Frontier Research Center funded by the U.S. Department of Energy, Office of Science under DOE (BES); Award DE-SC0019165.

Appendix. Analysis of specific images

In this appendix, we aim to offer additional analysis by delving deeper into the six selected images presented in Fig. 5(right). These examples were selected to show a broad range of geometric characteristics and how they impact transport, not to provide statistical coverage of the dataset; a more systematic grouping and analysis (e.g., clustering based on geometric features) could be the subject of future work.

To visualize how the effective dispersion tensor is calculated, Eq. (19) can be reformulated as:

$$\mathbf{D}^* = \langle \mathbf{d}^* \rangle, \tag{A.1}$$

where $\mathbf{d}^*(\mathbf{y})$ is defined throughout the unit cell as:

$$\mathbf{d}^* = \mathbf{D}\left(\mathbf{I} + \nabla_{\mathbf{y}} \chi(\mathbf{y})\right) + \varepsilon \mathrm{Pe} \chi(\mathbf{y}) \mathbf{k}(\mathbf{y}) \nabla_{\mathbf{x}} p_0. \tag{A.2}$$

This variable represents the dispersion pathways available at each point in the unit cell, and thus provides insight into the geometric features contributing to each component of the effective dispersion tensor. Fig. A.10 shows a plot of each component of $\mathbf{d}^*$ for Ex. 4 at Pe = 1000. The solid particles in this example create a tortuous pathway that directs flow predominantly in the vertical direction, which can be seen in the d^*_{22} plot as well as the off-diagonal component plots, d^*_{12} and d^*_{21}, where $d^*_{ij} = [\mathbf{d}^*]_{ij}$.

To compare the behavior of $\mathbf{d}^*$ across separate images, we show the diagonal components of this tensor for Ex. 5 and Ex. 6 at Pe = 1000 in Fig. A.11. These are the two lowest porosity examples considered. In Ex. 5, the particles block horizontal transport and direct flow and solute vertically. This preferential pathway becomes increasingly more dominant at high Pe, resulting in low values for d^*_{11} and high d^*_{22}. On the other hand, despite its low porosity, Ex. 6 features an unobstructed horizontal pathway, seen in the d^*_{11} component. Because of this low resistance channel aligned with the pressure gradient, d^*_{22} remains low even at high Pe.

For each example image, simulations were performed to investigate and visualize the transport behavior. The flow field for each unit cell was determined through the permeability closure problem and is depicted in Fig. 5(right). The north–south boundary conditions were set to be periodic, while the east–west boundary conditions were set as a periodic jump condition to allow for continuous injection—where the concentration on the west boundary, c_W, is determined from that at the east boundary, c_E, by:

$$c_W = 1 + c_E. \tag{A.3}$$

The simulations were conducted until reaching a time $t_A = 5$, which corresponds to the advective time scale, i.e. on average, particles traversed the unit cell five times. To explore different regimes of transport, simulations were run for $\mathrm{Pe} = (1, 10, 100, 1000)$. The Péclet number was set by keeping the velocity field constant and modifying the molecular diffusion coefficient D accordingly in each scenario. The simulations were run using the open-source *scalarTransportFoam* solver in OpenFOAM. The timestep is set in accordance with the Courant–Friedrichs–Lewy (CFL) stability condition, $\Delta t < \frac{l_{\min}}{2|\mathbf{u}_{\max}|}$, where $l_{\min}$ is the minimum grid size and $|\mathbf{u}_{\max}|$ is the maximum magnitude of velocity field in the grid, which is known from the permeability closure solution. Videos were created to visualize the concentration evolution over time. A static image of the final time step for Ex. 1 and Ex. 3 are shown in Fig. A.12. The concentration color map in these plots is periodic to cover a broad range of concentration values, while ensuring that the dynamics can still be visualized. Thus, the streamlines in these plots can be thought of as the contour lines. These examples are both high porosity images and display different dispersive behaviors as Pe is increased. At $\mathrm{Pe} = 1$, the concentration is well-mixed throughout the image for both Ex. 1 and Ex. 3. and the gradients are not very sharp as expected. This is in sharp contrast with the $\mathrm{Pe} = 1000$ case, particularly for Ex. 3, where D^*_{11} increases most rapidly. In this example, it can be seen that the solute has been driven repeatedly through the horizontal flow channel towards the top of the image and, at that location, the concentration values are very high at the final time step. However, limited mixing is experienced in the orthogonal (y_2-direction) and very sharp gradients in concentration exist as evidenced by the horizontally oriented laminae. This is consistent with a low D^*_{22} found through the solution of the closure problem.

Data availability

Data will be made available on request.

References

Auriault, J.-L., Adler, P.M., 1995. Taylor dispersion in porous media: analysis by multiple scale expansions. Adv. Water Resour. 18 (4), 217–226.

Auriault, J.-L., Moyne, C., Souto, H., 2010. On the asymmetry of the dispersion tensor in porous media. Transp. Porous Media 85, 771–783.

Battiato, I., Malley, D.O., Miller, C.T., Takhar, P.S., Valdes-Parada, F., Wood, B.D., 2019. Theory and applications of macroscopic models in porous media. Transp. Porous Media 13 (1), 1–72.

Battiato, I., Tartakovsky, D., 2011. Applicability regimes for macroscopic models of reactive transport in porous media. J. Contam. Hydrol. 120, 18–26.

Boelens, A.M., Tchelepi, H.A., 2021. QuantImPy: Minkowski functionals and functions with python. SoftwareX 16, 100823.

Boso, F., Battiato, I., 2013. Homogenizability conditions of multicomponent reactive transport processes. Adv. Water Resour. 62, 254–265.

Carbonell, R., Whitaker, S., 1983. Dispersion in pulsed systems—II: Theoretical developments for passive dispersion in porous media. Chem. Eng. Sci. 38 (11), 1795–1802.

Carman, P., 1997. Fluid flow through granular beds. Chem. Eng. Res. Des. 75, S32–S48.

Dejam, M., Hassanzadeh, H., 2022. Dispersion tensor in stratified porous media. Phys. Rev. E 105, 065115.

Gouze, P., Puyguiraud, A., Porcher, T., Dentz, M., 2021. Modeling longitudinal dispersion in variable porosity porous media: Control of velocity distribution and microstructures. Front. Water 3.

Graczyk, K., Matyka, M., 2020. Predicting porosity, permeability, and tortuosity of porous media from images by deep learning. Sci. Rep. 10 (21488).

Hanna, J.M., Aguado, J.V., Comas-Cardona, S., Le Guennec, Y., Borzacchiello, D., 2024. A self-supervised learning framework based on physics-informed and convolutional neural networks to identify local anisotropic permeability tensor from textiles 2D images for filling pattern prediction. Compos. Part A: Appl. Sci. Manuf. 179, 108019.

Hidalgo, J.J., Carera, J., 2009. Effect of dispersion on the onset of convection during CO2 sequestration. J. Fluid Mech. 640, 441–452.

Honari, A., Zecca, M., Vogt, S.J., Iglauer, S., Bijeljic, B., Johns, M.L., May, E.F., 2016. The impact of residual water on CH4-CO2 dispersion in consolidated rock cores. Int. J. Greenh. Gas Control. 50, 100–111.

Icardi, M., Boccardo, G., Marchisio, D.L., Tosco, T., Sethi, R., 2014. Pore-scale simulation of fluid flow and solute dispersion in three-dimensional porous media. Phys. Rev. E 90, 013032.

Ioffe, S., Szegedy, C., 2015. Batch normalization: accelerating deep network training by reducing internal covariate shift. ICML abs/1502.03167.

Kamrava, S., Im, J., de Barros, F., Sahimi, M., 2021. Estimating dispersion coefficient in flow through heterogeneous porous media by a deep convolutional neural network. Geophys. Res. Lett. 48.

Kamrava, S., Tahmasebi, P., Sahimi, M., 2020. Linking morphology of porous media to their macroscopic permeability by deep learning. Transp. Porous Media 131.

Kingma, D.P., Ba, J., 2015. Adam: a method for stochastic pptimization. Int. Conf. Learn. Represent..

Ling, B., Battiato, I., 2020. τ-SIMPLE algorithm for the closure problem in homogenization of stokes flows. Adv. Water Resour. 144, 103712.

Ling, B., Rizzo, C.B., Battiato, I., de Barros, F.P.J., 2021. Macroscale transport in channel-matrix systems via integral transforms. Phys. Rev. Fluids 6, 044501.

Ling, B., Tartakovsky, A.M., Battiato, I., 2016. Dispersion controlled by permeable surfaces: surface properties and scaling. J. Fluid Mech. 801, 13–42.

Lu, X., Giovanis, D., Yvonnet, J., Papadopoulos, V., Detrez, F., Bai, J., 2019. A data-driven computational homogenization method based on neural networks for the nonlinear anisotropic electrical response of graphene/polymer nanocomposites. Comput. Mech. 64, 307–321.

Marafini, E., Rocca, M.L., Firoi, A., Battiato, I., Prestininzi, P., 2020. Suitability of 2D modelling to evaluate flow properties in 3D porous media. Transp. Porous Media 134, 315–329.

Marcato, A., Boccardo, G., Marchisio, D., 2021. A computational workflow to study particle transport and filtration in porous media: Coupling CFD and deep learning. Chem. Eng. J. 417, 128936.

Marcato, A., Boccardo, G., Marchisio, D., 2022. From computational fluid dynamics to structure interpretation via neural networks: An application to flow and transport in porous media. Ind. Eng. Chem. Res. 61 (24), 8530–8541.

Marcato, A., Santos, J.E., Boccardo, G., Viswanathan, H., Marchisio, D., Prodanović, M., 2023. Prediction of local concentration fields in porous media with chemical reaction using a multi scale convolutional neural network. Chem. Eng. J. 455, 140367.

Marušić-Paloka, E., Piatnitski, A.L., 2005. Homogenization of a nonlinear convection-diffusion equation with rapidly oscillating coefficients and strong convection. J. Lond. Math. Soc. 72 (2), 391–409.

Meigel, F., Darwent, T., Bastin, L., Goehring, L., Alim, K., 2022. Dispersive transport dynamics in porous media emerge from local correlations. Nat. Comm. 13, 5885.

Mianroodi, J., Rezaei, S., Siboni, N., Xu, B.-X., Raabe, D., 2022. Lossless multi-scale constitutive elastic relations with artificial intelligence. Npj Comput. Mater. 8, 67.

Mikelic, A., Devigne, V., Duijn, C.J.V., 2006. Rigorous upscaling of the reactive flow through a pore, under dominant peclet and damkohler numbers. SIAM J. Math. Anal. 38 (4), 1262–1287.

Nguyen, V., Papavassiliou, D., 2020. Hydrodynamic dispersion in porous media and the significance of Lagrangian time and space scales. Fluids 5, 79.

Nitsche, L.C., Brenner, H., 1989. Eulerian kinematics of flow through spatially periodic models of porous media. Arch. Ration. Mech. Anal. 107, 225–292.

Pietrzyk, K., Battiato, I., 2023. Automated symbolic upscaling: 1. Model generation for extended applicability regimes. Water Resour. Res. e2022WR033600.

Pietrzyk, K., Korneev, S., Behandish, M., Battiato, I., 2021. Upscaling and automation: pushing the boundaries of multiscale modeling through symbolic computing. Transp. Porous Media 140 (1).

Pride, S.R., Vasco, D.W., Flekkoy, E.G., Holtzman, R., 2017. Dispersive transport and symmetry of the dispersion tensor in porous media. Phys. Rev. E 95, 043103.

Rao, C., Liu, Y., 2020. Three-dimensional convolutional neural network (3D-CNN) for heterogeneous material homogenization. Comput. Mater. Sci. 184, 109850.

Rubol, S., Battiato, I., de Barros, F.P.J., 2016. Vertical dispersion in vegetated shear flows. Water Resour. Res. 52 (10), 8066–8080.

Špetlík, M., Březina, J., Laloy, E., 2024. Deep learning surrogate for predicting hydraulic conductivity tensors from stochastic discrete fracture-matrix models. Comput. Geosci. 28, 1425–1440.

Srivastava, N., Hinton, G., Krizhevsky, A., Sutskever, I., Salakhutdinov, R., 2014. Dropout: A simple way to prevent neural networks from overfitting. J. Mach. Learn. Res. 15 (1), 1929–1958.

Taghizadeh, E., Byrne, H.M., Wood, B.D., 2022. Explicit physics-informed neural networks for nonlinear closure: The case of transport in tissues. J. Comput. Phys. 449, 110781.

Tang, P., Zhang, D., Li, H., 2022. Predicting permeability from 3D rock images based on CNN with physical information. J. Hydrol. 606, 127473.

van Milligen, B., Bons, P., 2012. Analytical model for tracer dispersion in porous media. Phys. Rev. E Stat. Nonlinear Soft Matter Phys. 85, 011306.

Wall, P., 2007. Homogenization of Reynolds equation by two-scale convergence. Chin. Ann. Math. Ser. B 28 (3), 363.

Wang, Y.D., Blunt, M., Armstrong, R., Mostaghimi, P., 2021a. Deep learning in pore scale imaging and modeling. Earth- Sci. Rev. 215.

Wang, H., Yin, Y., Hui, X., Bai, J., Qu, Z., 2020. Prediction of effective diffusivity of porous media using deep learning method based on sample structure information self-amplification. Energy AI 2, 100035.

Wang, D., Zhang, X., Zhang, J., Cheng, L., 2021b. A simulation study on the effect of the dispersion on the process of enhanced oil recovery. IOP Conf. Ser.: Earth Environ. Sci. 675, 012204.

Weber, R.M., Korneev, S., Battiato, I., 2022. Homogenization-informed convolutional neural networks for estimation of li-ion battery effective properties. Transp. Porous Media 145.

Weber, R.M., Ling, B., Battiato, I., 2024. Enforcing global constraints for the dispersion closure problem: τ^2-SIMPLE algorithm. Adv. Water Resour. 191, 104759.

Wood, B.D., 2007. Inertial effects in dispersion in porous media. Water Resour. Res. 43 (12).

Wu, H., Fang, W., Kang, Q., Tao, W., Qiao, R., 2019. Predicting efective diffusivity of porous media from images by deep learning. Sci. Rep. 9 (20387).

Yang, X., Mehmani, Y., Perkins, W.A., Pasquali, A., Schönherr, M., Kim, K., Perego, M., Parks, M.L., Trask, N., Balhoff, M.T., Richmond, M.C., Geier, M., Krafczyk, M., Luo, L.-S., Tartakovsky, A.M., Scheibe, T.D., 2016. Intercomparison of 3D pore-scale flow and solute transport simulation methods. Adv. Water Res. 95, 176–189.

Yang, Z., Yabansu, Y.C., Al-Bahrani, R., keng Liao, W., Choudhary, A.N., Kalidindi, S.R., Agrawal, A., 2018. Deep learning approaches for mining structure-property linkages in high contrast composites from simulation datasets. Comput. Mater. Sci. 151, 278–287.